Detection and characterization of attenuated multimode waveguiding in SiO_2 slabs using photoemission electron microscopy

Alwin Klick,[1,*] René Wagner,[1] Malte Großmann,[1] Laith F. Kadem,[2] Till Leißner,[3] Horst-Günter Rubahn,[3] Christine Selhuber-Unkel,[2] and Michael Bauer[1]

[1]*Institute of Experimental and Applied Physics, University of Kiel, Leibnizstr. 19, D-24118 Kiel, Germany*

[2]*Institute for Materials Science, University of Kiel, Kaiserstr. 2, D-24143 Kiel, Germany*

[3]*Mads Clausen Institute, NanoSYD, University of Southern Denmark, Alsion 2, DK-6400 Sønderborg, Denmark*

(Received 3 November 2017; published 16 August 2018)

Multimode waveguiding in the visible and near-ultraviolet spectral regime is observed and characterized in thermally grown SiO_2 layers on silicon using photoemission electron microscopy (PEEM). Comparison with finite-element-method simulations allows identifying order and character of the attenuated modes. Real-time investigations on mode propagation support these findings and give additional evidence for the existence of radiative modes. Finally, the presented experimental results illustrate how a defined deposition of gold nanoparticles can substantially enhance the sensitivity of the PEEM technique to electromagnetic field modes supported by thin dielectric and insulating layers.

DOI: 10.1103/PhysRevB.98.085128

I. INTRODUCTION

In recent years, photoemission electron microscopy (PEEM) has emerged as a powerful near-field probe for studying propagating electromagnetic modes confined to the surface or near-surface region of conducting samples. The technique provides an exceptional lateral resolution in the order of 10 nm and below [1]. Additionally, when operated in a time-resolved mode, it allows monitoring in real-time processes taking place on a few-fs timescale [2,3]. Most PEEM studies focused so far on surface plasmon polaritons (SPP) supported by metal-dielectric interfaces. Topics included SPP phase and group propagation [4–7], SPP dispersion [8,9], plasmonic focusing [10,11] and switching [12], plasmonic waveguiding [13,14], and the formation of plasmonic vortices [15].

Recently, it was shown that PEEM can be used in a similar manner to map optical waveguide modes supported by dielectric layers [16–19] and their manipulation by photonic structures [20]. The dielectric material of choice in these studies was indium tin oxide owing to its well-known conductive properties which are intrinsically required to perform photoemission-based experiments. As dielectric properties are key parameters for the design of photonic structures, it would be highly desirable if the unique capabilities of the PEEM technique could also be applied to nonconducting materials which are more commonly used in optical waveguide applications.

In this paper, we report on the observation and characterization of optical waveguide modes in SiO_2 slabs of different thickness using PEEM. Two key ingredients allow mapping the modes confined in the insulating slabs: internal photoemission from an underlying silicon substrate guarantees charge neutrality during the experiments. Furthermore, gold nanoparticles deposited on top of the waveguide act as efficient electron emitters sensing the near field at the surface generated by the waveguide modes. In addition, interferometric time-resolved PEEM experiments were performed which allow monitoring in real time the propagation of excited waveguide modes, in a very similar manner to what was reported in the past for SPPs [4]. Notably, the time-resolved data allow identifying a radiative mode of the slab which keeps hidden in the static PEEM data.

II. EXPERIMENTAL SETUP

The experiments were conducted using a photoemission electron microscope (IS PEEM, *Focus GmbH*) [21] mounted in an ultrahigh vacuum (UHV) μ-metal chamber and providing a lateral resolution of 40 nm. Available light sources for static PEEM experiments were the 254-nm ($h\nu = 4.9$ eV) main emission line of a mercury discharge lamp and the second and fourth harmonics of the pulsed near-infrared output of a Ti:sapphire oscillator [Tsunami, *Spectra Physics*, tuning range: 710 to 890 nm, 40-fs pulse width (FWHM)]. The second harmonic light covered a wavelength range between 360 and 430 nm ($h\nu = 3.45$ and 2.89 eV, respectively) and was used to perform PEEM experiments in the two-photon photoemission mode (2PPEEM) [2]. Fourth harmonic light was generated by frequency doubling of 420-nm ($h\nu = 2.95$ eV) second harmonic pulses providing a wavelength λ of 210 nm ($h\nu = 5.9$ eV). Photon energies of fourth harmonic and mercury lamp resulted in one-photon photoemission from the investigated samples and generated, therefore, conventional threshold PEEM (TPEEM) images. Prior to the PEEM experiments, wavelengths of second and fourth harmonic were measured using a calibrated fiber optic spectrometer (USB4000, Ocean Optics) in front of the UHV chamber entrance window.

*klick@physik.uni-kiel.de

Interferometric time-resolved 2PPEEM (ITR-2PPEEM) experiments were conducted using the second harmonic of a sub-15-fs Ti:sapphire oscillator (Griffin, *KMLabs*, 800 nm). 15-fs pulses with a central wavelength of 400 nm ($h\nu = 3.1$ eV) were split into two identical pulses using an actively stabilized Mach-Zehnder interferometer [22]. The stability of the interferometer allowed adjusting the temporal delay between the two excitation laser pulses with a timing accuracy of better than 30 as [5]. All laser-based experiments were performed with p-polarized pulses hitting the sample at an angle of incidence $\Theta = 65^\circ$ with respect to the surface normal.

Scanning electron microscopy (SEM) and helium ion microscopy (HIM) were used to map the sample surface. SEM experiments were performed using a Hitachi S-4800 microscope. HIM was carried out by an Orion NanoFab helium ion microscope (Carl Zeiss) at 30-keV beam energy, with an applied probe current ranging from 0.5 to 1.1 pA.

III. SAMPLES

Sample preparation followed a process described in detail in Ref. [23]. Silicon wafers with a thermally grown, 1.5 μm ± 5% oxide layer were microstructured using photolithography and wet etching as follows: 25-μm-wide and 60-nm-deep stripes, separated by 25 μm, were etched into the oxide layer. The process was repeated after rotation of the sample by 90°, resulting in a quadruple, checkerboardlike pattern with segments of different heights of the SiO_2 layer [see Fig. 1(a)]. At illumination with light, the segment edges of the platforms act as momentum source required to overcome the wave-vector mismatch between light and the waveguide modes supported by the SiO_2 layer. The sample design allows, furthermore, studying three different waveguide geometries in parallel.

Using block copolymer micelle nanolithography, the SiO_2 surface was additionally decorated with gold nanoparticles with a nominal size of 5–8 nm in diameter. In detail, a gold-carrying micelle solution is spin coated onto the microstructure, where the micelles self-assemble into a quasihexagonal structure with an inter-particle distance of 50–100 nm. Afterwards, the polymer micelles are removed via plasma etching, leaving the metallic gold nanoparticles. As will be shown below, the decoration of the SiO_2 surface with gold nanoparticles is essential for observation and characterization of waveguide modes using PEEM.

Figure 1(b) shows an SEM image of a sample after deposition of gold nanoparticles. The obvious difference in the nanoparticle density between different segments was discussed in detail in an earlier study [23]. For instance, the particle density observed in the top right segment is much more sparse than in the bottom left segment. The corresponding slab heights are 1.5 and 1.38 μm, respectively. Furthermore, in the vicinity of the segment edges one observes a gradient in the nanoparticle density with a decrease in density when approaching an edge from the upper level and an increase in density when approaching an edge from the lower level. In this border region, the average gold interparticle distance varies between ≈50 and ≈150 nm. The overall difference in nanoparticle density between the different segments decreases towards the respective field centers, where no difference in nanoparticle density between different segments is observed any more. The approximate gold interparticle distance in this region is ≈60 nm. HIM images were taken to additionally gain information on the size of the deposited particles. The data show that the diameter of the deposited nanoparticles is smaller than 15 nm.

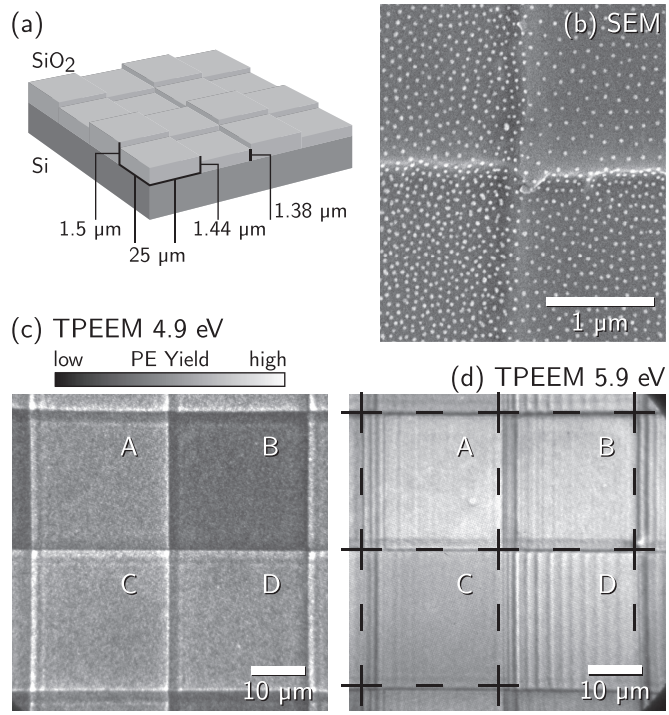

FIG. 1. (a) Schematic of the sample geometry; relevant dimensions are indicated. (b) SEM image of a sample showing the intersection of four segments; individual gold nanoparticles appear as bright spots. (c) TPEEM image of four segments recorded at illumination with the Hg discharge lamp ($h\nu = 4.9$ eV). (d) TPEEM image of four segments recorded at illumination with the fourth harmonic laser light ($h\nu = 5.9$ eV, laser incident from the left); dashed lines indicate the borders of the individual segments, which were determined by comparison with TPEEM data recorded with the Hg discharge lamp. Note the different scale bars in (b) and (c) and (d), respectively.

IV. STATIC PEEM RESULTS

Figures 1(c) and 1(d) show images of four neighboring sample segments recorded in TPEEM mode using 254-nm light (Hg discharge lamp) and 210-nm light (laser fourth harmonic), respectively. Despite the presence of a rather thick and insulating layer of SiO_2 sharp images of the sample surface using low kinetic energy ($\leqslant$2 eV) photoelectrons can be recorded. Notably, sharp PEEM images can also be recorded from samples which were not decorated with gold nanoparticles [see Fig. 7(a)]. We suspect that internal photoemission (IPE) from the valence band of the silicon substrate into the SiO_2 conduction band delivers compensation charges preventing image distortion or a complete blocking of the photoemission process due to surface charging [24–26]. A photon energy threshold of 4.3 eV for IPE at the Si/SiO_2 interface was reported before [26], making IPE possible in a one-photon absorption process on excitation with fourth harmonic light and the Hg discharge lamp and in a two-photon absorption process on excitation with the second harmonic light. The

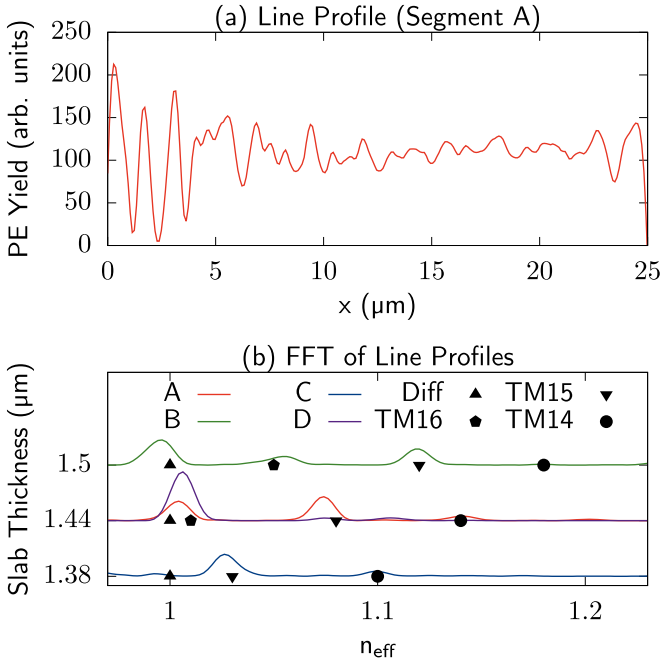

FIG. 2. (a) PE intensity profile across segment A in Fig. 1(d); (b) FFT spectra of the PE intensity profiles across the different segments labeled A–D in Fig. 1(d); the black symbols are FEM results for effective indices of the slab waveguide modes. "Diff" denotes the diffracted, quasicylindrical mode, whereas "TMX" indicates the transverse magnetic waveguide mode of order X.

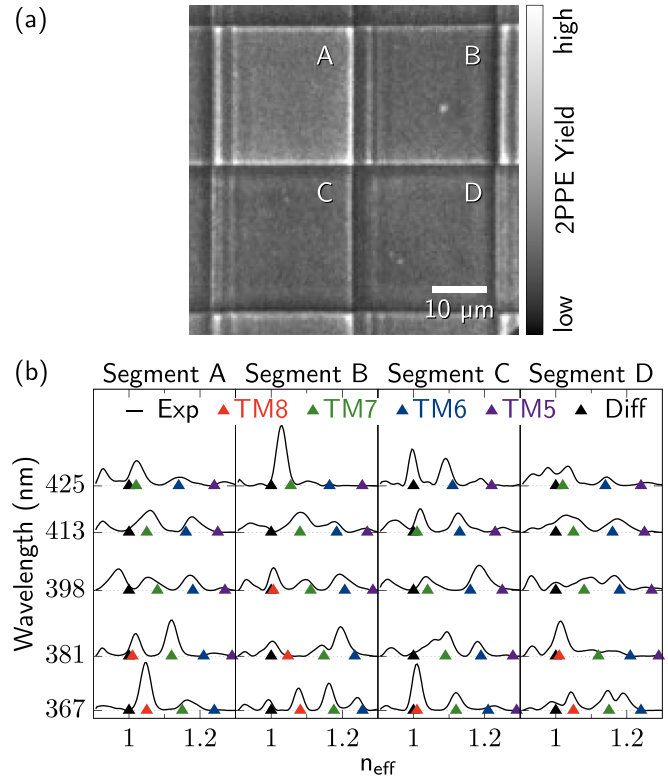

FIG. 3. (a) 2PPEEM image of the sample illuminated with 400-nm laser light; the sample is illuminated with the laser light incident from the left. (b) FFT spectra of 2PPE intensity profiles across the four segments in Fig. 2(a) for different excitation wavelengths; black and colored triangles mark effective mode indices obtained from the FEM simulations. $n_{\text{eff}} = 1$ (black triangles) indicates the incident laser mode which is diffracted at the coupling edge (quasicylindrical mode). Red, green, blue, and purple triangles mark the position of the TM8, TM7, TM6, and TM5 waveguide modes supported by the SiO_2 slab, respectively.

TPEEM image recorded with 254-nm light shows a clear correlation between photoemission yield and height of SiO_2 layer: the highest segment [upper right segment in Fig. 1(c)] appears darker, while the lowest segment (lower left segment) appears brighter than the two intermediate segments. This correlation allows for an unambiguous assignment of the SiO_2 layer thickness to the individual segments as mapped in the PEEM experiments.

On excitation with 210-nm light [Fig. 1(d)] we observe strongly modulated periodic photoemission intensity patterns emerging from the left-hand edges covering the entire area of the individual segments. Similar intensity modulations, albeit more restricted to the vicinity of the coupling edges, are also observed on excitation with 400-nm light [Fig. 3(a)]. The observation of periodic intensity patterns in PEEM is a characteristic signature for propagating electromagnetic modes which were excited at the sample surface. In the past, such patterns have been associated with the excitation of surface plasmon polaritons at metal-dielectric interfaces [4] and guided optical modes within dielectric slabs [16]. The pattern formation results from the coherent superposition of illuminating light field and phase-coupled surface mode or waveguide mode with the periodicity given by the wave-vector mismatch $\Delta k = |k_l - k_{ex}|$ [4]. k_l denotes here the surface projected wave vector of the illuminating light field, i.e., $k_l = {}^{2\pi}/_{\lambda} \sin\Theta$, k_{ex} is the wave vector of the excited mode. The pattern contrast depends on the order of the photoemission process and is given by $(1+\beta)^2/(1-\beta)^2$ in the case of a one-photon photoemission process and by $(1+\beta)^4/(1-\beta)^4$ in the case of a two-photon photoemission process [27]. Here, β denotes the ratio of the normal components of mode electric field amplitude and laser electric field amplitude.

Figure 2(a) shows the photoemission (PE) intensity profile of the upper left segment in Fig. 1(d), in the following referred to as segment A (see also labeling of the PEEM images). The shape of the profile hints to more than one periodicity involved in the formation of the intensity pattern. A Fourier analysis allows for a quantitative interpretation of such PEEM patterns [16–20]. A fast Fourier transformation (FFT) of the photoemission intensity profiles of all four segments was performed using the Welch method [28] [Fig. 2(b)]. The graphs display FFT power spectral densities as function of the mode effective index

$$n_{\text{eff}} = \frac{k_{ex}}{k_l}. \tag{1}$$

Each spectrum shows several peaks which we associate with the excitation of different modes by the illuminating laser pulse. Reasonable agreement in the peak position is observed for segments A and D, which exhibit the same SiO_2 layer thickness of 1.44 μm. The Fourier analysis of the 2PPEEM patterns yield very similar results. Figure 3(b) compares FFT spectra of the four segments and for five different excita-

tion wavelengths. Once again, the spectra clearly prove the multimode character of the excitation. Again, the spectra of segments A and D match rather well. The comparison of the data recorded with different excitation wavelengths hint, furthermore, to a dispersive character of the individual modes as expected for propagating modes.

In an optical waveguide, the effective index of a waveguide mode is given by

$$n_{\text{eff}} = n \sin \vartheta, \tag{2}$$

with n being the refractive index of the waveguide material and ϑ being the mode propagation angle with respect to the normal of the waveguide supporting interfaces. For a self-consistent solution of Eq. (2), ϑ has to fulfill the relation [29]

$$2\pi m = 2k_0 nd \cos \vartheta + \phi_1 + \phi_1. \tag{3}$$

Here, m is an integer and typically referred to as the mode order, $k_0 = \omega/c_0$ the vacuum wave vector, with ω being the mode frequency, and d the thickness of the waveguide. Finally, ϕ_1 and ϕ_2 are the phase shifts experienced by the mode at reflection at the mode supporting interfaces. Equations (2) and (3) directly imply that in the experiments a dependence of n_{eff} on excitation wavelength as well as SiO_2 slab thickness are to be expected.

To verify the detection of optical waveguide modes supported by the SiO_2 layer, we performed finite-element-method (FEM) simulations for comparison with the experimental data. The FEM calculations were carried out using the wave optics module of COMSOL MULTIPHYSICS. According to the sample geometry we considered in the calculations two-dimensional SiO_2 slabs of 1.5-, 1.44-, and 1.38-μm thickness which were sandwiched in-between a silicon substrate and a vacuum superstrate. The model did not account for the deposited gold nanoparticles. FEM calculations were performed for all excitation wavelengths investigated in the study resulting in a plethora of mathematical solutions to the relevant boundary condition problem. Each solution provides relevant mode parameters such as effective mode index and electric and magnetic field profile. Only some of these solutions represent actual waveguide modes. One has to closely examine the effective mode indices and mode field profiles in order to distinguish between waveguide modes and other, nonwaveguiding modes or potentially nonphysical modes. Of the waveguide modes, only transverse magnetic (TM) modes were considered for comparison with the experimental data since only those can be excited with p-polarized light. The results of the FEM calculations for the photon energy range accessible in the 2PPEEM experiments are summarized in the mode dispersion diagram shown in Fig. 4(a). The solid lines represent the light line in vacuum and SiO_2, respectively, i.e., photon energy as function of wave vector. Only modes located to the right of the vacuum light line, i.e., modes with $n_{\text{eff}} > 1$, undergo total internal refraction at the SiO_2/vacuum interface and can be considered as waveguide modes. These modes are, however, partially refracted into the silicon substrate due to the refractive index of silicon being larger than the refractive index of SiO_2. These losses result in a considerable attenuation of the modes and correspondingly short propagation lengths. In the wavelength range accessible by the second harmonic of the laser output, an overall of 8 TM waveguide modes

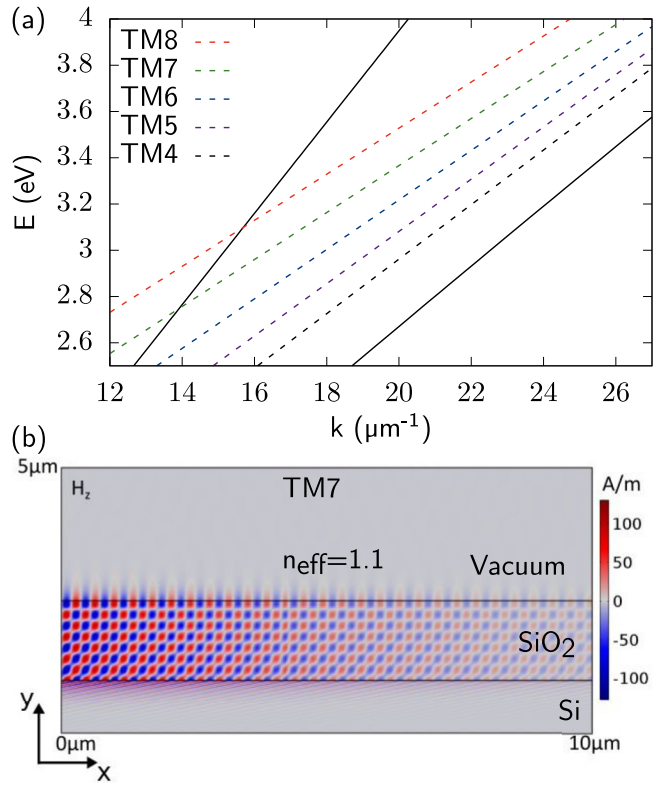

FIG. 4. (a) Mode dispersion diagram compiled from the results of the FEM calculations; the solid black and gray lines represent the light line in vacuum and SiO_2, respectively. Colored dashed lines represent TM waveguide modes. (b) Calculated magnetic field amplitude of the TM7 mode for excitation with 400-nm light and a slab thickness of 1.5 μm.

are identified, at excitation with fourth harmonic light the calculation yields 16 TM modes.

Figure 4(b) shows results of the calculations for the magnetic field amplitude of the TM7 mode, i.e., the TM mode exhibiting seven nodes across the SiO_2 slab. The slab thickness is 1.5 μm and the excitation wavelength is 400 nm. For the effective index of the mode, the calculation yields a value of $n_{\text{eff}} = 1.1$. Due to the radiation losses into the silicon substrate, the propagation length is restricted to $\approx$2.5 μm. The mode propagation lengths in the UV spectral regime are predicted to be longer. For instance, for the TM16 mode the simulations yield a value of $\approx$4.5 μm. The decay lengths of the corresponding superposition signal as probed in the PEEM experiments [Figs. 1(d) and 3(a)] at the least qualitatively confirm these numbers.

FEM results for effective indices of different modes and for the different slab thicknesses are added for comparison with the experimental data to Figs. 2(b) and 3(b). On excitation with 210-nm light, the highest-order mode supported by the SiO_2 slabs (yielding the lowest n_{eff}) is the TM16 mode, on excitation at wavelengths of $\approx$400 nm the highest-order mode is the TM8 mode. The comparison of experimental data and simulation shows a good to very good quantitative agreement, both for the TPEEM results as well as the 2PPEEM results, proving that the experiments indeed probe propagating waveguide modes in the SiO_2 slabs. Based on the comparison between

experiment and simulation, it would be possible to identify the respective segments in terms of layer thickness or, even more, to determine the layer thickness with an accuracy in the 10-nm range. Also, the changes in n_{eff} as function of excitation wavelength, i.e., the dispersion relations of the modes as probed in the 2PPEEM experiment, are very well reproduced by the FEM calculations. Overall, we observe a reduction of the experimental mode amplitude with decreasing mode order. It results from the decrease of the coupling efficiency as at the same time the wave-vector mismatch with respect to the excitation laser pulse increases. Deviations from this behavior may arise from differences in the near-surface amplitude of the mode electric fields which are probed by the surface-sensitive PEEM technique [19]. Additionally, structural imperfections of the coupling edge for instance due to the presence of the gold nanoparticles could selectively affect the coupling efficiency for a specific mode. The lowest-order mode visible in the experimental data is the TM5 mode.

In some of the experimental spectra, an extra peak shows up at $n_{\mathrm{eff}} = 1$. The experiment probes here the incident laser mode which is diffracted at the step edge and which in literature is often referred to as "quasicylindrical wave" [30–34].

For a multimode excitation scenario as in the present case, the appearance of a periodic intensity pattern in the PEEM data could alternatively arise from the superposition of two different waveguide modes [16]. The periodicity of the pattern will then be given by the wave-vector mismatch between the coupled modes, yielding additional peaks in the Fourier spectra. The experimental data do not show distinct indications for such an additional signal. We suspect that the excited mode amplitudes are too small to compete with the primary PEEM signal arising from the superposition of incident laser field and waveguide modes.

Indications for backward propagating modes, i.e., modes which propagate in opposite direction with respect to the incident laser field, were observed neither on excitation with second harmonic light nor on excitation with fourth harmonic light. In the used excitation geometry, the coupling efficiency for these types of modes is strongly reduced in comparison to the observed forward propagating modes as was shown in the past for instance in the case of backward propagating SPP modes supported by a gold vacuum interface [5,35].

V. TIME-RESOLVED PEEM RESULTS

Figure 5(a) shows four ITR-2PPEEM intensity profiles of segment D (SiO_2 layer thickness: 1.44 μm) recorded within a single optical cycle of the excitation laser pulse at a temporal delay τ of 27.7 fs and at incremental steps of 0.3 fs. A complete movie covering an overall delay range of 10–45 fs is in addition added in the Supplemental Material [36]. The overall response of the 2PPEEM signal from the attenuated waveguide modes to changes in the temporal delay is very similar to what was reported in the past in ITR-2PPEEM studies on the propagation dynamics of SPPs [4,10]: within an optical cycle, we observe a forward motion of the superposition maxima (and minima) towards the center of the segment which arises from the phase propagation of the detected modes.

Delay-distance diagrams as shown for segment D in Fig. 5(b) allow illustrating the mode propagation dynamics in

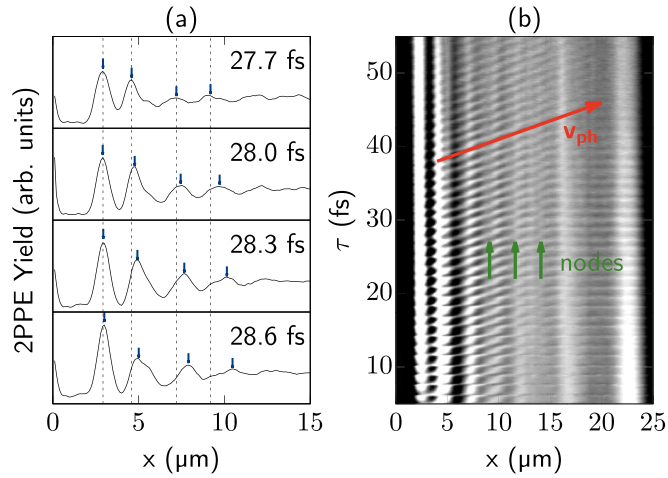

FIG. 5. (a) ITR-2PPEEM intensity profiles of segment D at different time delays recorded within one optical cycle of the excitation laser; the time delays correspond to incremental phase delays of $\approx\pi/2$; blue arrows mark the position of interference maxima, starting positions of the maxima are marked with gray lines; (b) delay-distance diagram of segment D generated from the ITR-2PPEEM scan; the red arrow marks the slope of the interference maxima associated with the phase propagation of the TM7 mode. Green arrows mark beating nodes arising from the superposition of the TM7 mode and propagating lower-order modes.

a single image. The figure displays photoemission intensity profiles generated by vertical integration across segment D as a function of τ and propagation distance x. The overall signal quality particularly allows for a quantitative evaluation of the phase velocity v_{ph} of the main mode contributing to the signal. In the delay-distance representation, the propagation of superposition maxima and minima is transformed into alternating bright and dark streaks. v_{ph} determines the slope $\frac{\partial\tau}{\partial x}$ of the streaks and can be evaluated as follows [5]:

$$v_{\mathrm{ph}} = \left[\frac{\partial\tau}{\partial x} + \frac{\sin\Theta}{c}\right]^{-1}.$$

Accordingly, the effective mode index is given by

$$n_{\mathrm{eff}} = \sin\Theta + c\frac{\partial\tau}{\partial x}. \tag{4}$$

For segment D, Eq. (4) yields an effective mode index of $n_{\mathrm{eff}} = 1.07$, a value which agrees very well with the FEM result for the TM7 mode, i.e., the lowest-index waveguide mode excited at 400-nm laser wavelength. Data analysis of the other segments shows that the ITR-2PPEEM signal is in all cases dominated by the lowest-index waveguide mode. Higher-index modes show up as beating nodes in the delay-distance diagrams as marked in Fig. 5(b) by the green arrows.

Figure 6(a) compares ITR-2PPEEM intensity profiles of segment A (SiO_2 layer thickness: 1.44 μm) which were simultaneously recorded with the data of segment D shown in Fig. 5(a). Clearly visible is once again a forward propagation of superposition maxima arising from the phase propagation of the TM7 mode. Notably, in the close vicinity of the coupling edge an additional photoemission intensity maximum shows up which exhibits an inverted response as τ increases. Instead of a forward propagation towards the center of the

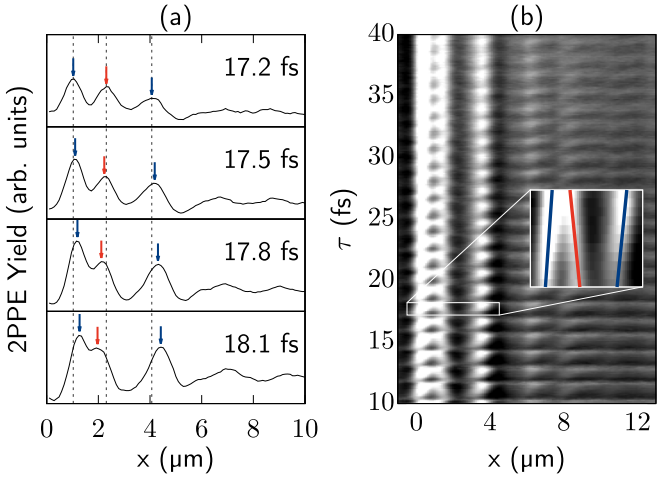

FIG. 6. (a) ITR-2PPEEM intensity profiles of segment A at time delays within one optical cycle of the excitation laser pulse; blue and red arrows mark the position of interference maxima, gray lines additionally mark the interference maxima in the first panel. (b) Delay-distance diagram of segment A generated from the ITR-2PPEEM scan; the inset shows a closeup of the region marked by the white box. The red line in the inset marks the negative slope $\frac{d\tau}{dx}$ of the interference maxima associated with a radiative mode of the SiO_2 slab. Blue lines mark for comparison the positive slope $\frac{d\tau}{dx}$ of interference maxima associated with the dominating nonradiative mode.

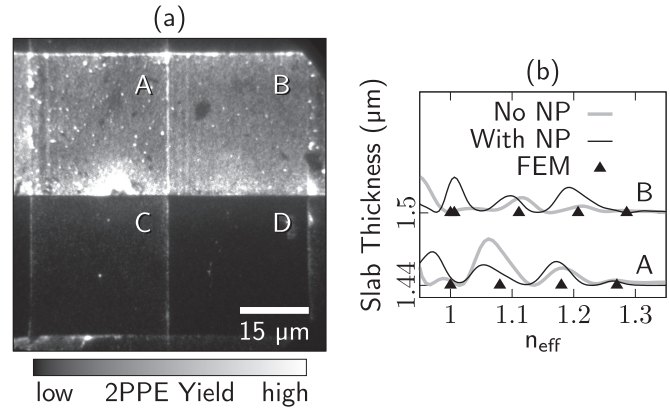

FIG. 7. (a) 2PPEEM image of a sample which was not covered with gold nanoparticles (NP); the image was recorded with 400-nm laser light. (b) FFT power spectral density of the 2PPE intensity profile of segments A and B in (a) in comparison to corresponding data from a nanoparticle covered surface and the results of the FEM simulations.

segment, we observe here a backward propagation towards the coupling edge. In the time-distance diagram [Fig. 6(b)], the corresponding interference streaks exhibit a negative slope $\frac{\partial\tau}{\partial x}$ (see red marker in the inset) yielding an effective mode index $n_{\text{eff}} < 1$, according to Eq. (4). Based on the experimental data, we estimate the value of the effective mode index to $n_{\text{eff}} \approx 0.6$. This result implies that the signal is due to a radiative mode which is subject to losses by refraction into the vacuum, i.e., a mode which is located to the left of the light line in Fig. 4(a). This interpretation is in line with the observation that a mode signal can only be observed in the very close vicinity of the coupling edge. Even though less pronounced, such a mode can also be noticed in segments B and C (see movie in the Supplemental Material [36]).

As the static 2PPEEM experiments provide only information on the absolute value of Δk, a mode with $n_{\text{eff}} = 0.6$ (corresponding to $\Delta k = 0.3\, k_L$) cannot be distinguished from a mode with $n_{\text{eff}} = 1.2$ [see Eq. (1)]. A distinct assignment of the mode character relies on the specific capabilities of ITR-2PPEEM.

VI. ROLE OF GOLD NANOPARTICLES

The role of the gold nanoparticles, which were deposited on top of the SiO_2 surface, have not been discussed in detail, yet. In the first instance, one could speculate if the particle arrays may also support propagating modes which can form from dipole-dipole interaction of neighboring particles following a polarization by the excitation laser pulse [37]. A quantitative analysis under consideration of particle size and particle arrangement shows that this cannot be the case in the relevant frequency range. This finding is supported by the very good agreement of the experimental data with the FEM simulations, which exclusively consider propagating modes in the SiO_2 slab.

The relevance of the nanoparticles for the experiments becomes evident from 2PPEEM images of nondecorated samples as shown in Fig. 7(a). Here, the data show significant irregularities particularly at the coupling edges and a strong contrast among different segments which is no longer linked to the SiO_2 layer thickness. Furthermore, the overall photoemission signal is significantly reduced in comparison to, for instance, the data shown in Fig. 3(a) so that for identical microscope settings the image integration time had to be increased by a factor of 20. Most importantly, if at all, only very weak signatures from the waveguide modes are visible making a quantitative data evaluation difficult. A reasonable FFT analysis of the 2PPEEM data in Fig. 7(a) is only possible for segments A and B: Fig. 7(b) shows FFT power spectral densities of the segments as function of n_{eff} in comparison to corresponding data from a nanoparticle covered sample and the results of the simulations. Within the accuracy of the evaluation, the agreement of the different data sets indicates an insignificant influence of the nanoparticles on the mode effective indices. Due to the limited data quality, an evaluation of PEEM data from the uncovered surface in the UV spectral regime was not possible.

The gold nanoparticles obviously act as efficient electron emitters probing the local field generated at the SiO_2 surface by the superposition of laser field and excited waveguide modes. The used photon energies imply that electron emission results from photoemission processes (and two-photon photoemission processes, respectively) initiated by the superposition field with the gold sp states close to the Fermi energy acting as initial states.

VII. CONCLUSION

PEEM was demonstrated before to be a viable instrument for the observation and characterization of optical guided modes [16,18,20]. Here, we showed that such investigations do not have to be restricted to conductive materials but that even an optical waveguide made from a very good insulator

can be studied in a comprehensive manner. To this end, the mode supporting material, SiO_2, was grown upon a silicon wafer to facilitate IPE. This in turn provided compensation charges necessary to avert image distorting charging during PEEM experiments. Gold nanoparticles deposited on top of the waveguide acted in addition as local antennas amplifying the evanescent mode electric field and translating it into a photocurrent detectable by the PEEM instrument. Notably, owing to the sparse coverage of a few percent and excitation conditions far off any (plasmonic) resonance, the effect of the nanoparticles on the mode spectrum is negligible, as confirmed by comparison of the experimental data with FEM simulations. We finally would like to emphasize the capabilities of the ITR-2PEEM technique which in this study was applied to investigate in real-time the propagation of optical waveguide modes and enabled us to unambiguously distinguish between guided and radiative modes of the SiO_2 slab.

ACKNOWLEDGMENTS

This work was supported by the German Research Foundation (DFG) through the Collaborative Research Center 677 "Function by Switching." We thank J. Adam for helpful discussion. C.S. and L.F.K. acknowledge funding from the European Research Council (ERC Starting Grant No. 336104).

[1] E. Bauer, *Surface Microscopy with Low Energy Electrons* (Springer, New York, 2014).
[2] O. Schmidt, M. Bauer, C. Wiemann, R. Porath, M. Scharte, O. Andreyev, G. Schönhense, and M. Aeschlimann, Appl. Phys. B **74**, 223 (2002).
[3] A. Kubo, K. Onda, H. Petek, Z. Sun, Y. S. Jung, and H. K. Kim, Nano Lett. **5**, 1123 (2005).
[4] A. Kubo, N. Pontius, and H. Petek, Nano Lett. **7**, 470 (2007).
[5] C. Lemke, T. Leißner, S. Jauernik, A. Klick, J. Fiutowski, J. Kjelstrup-hansen, H.-G. Rubahn, and M. Bauer, Opt. Express **20**, 12877 (2012).
[6] P. Kahl, S. Wall, C. Witt, C. Schneider, D. Bayer, A. Fischer, P. Melchior, M. H.-v. Hoegen, M. Aeschlimann, and F.-J. M. zu Heringdorf, Plasmonics **9**, 1401 (2014).
[7] Y. Gong, A. G. Joly, D. Hu, P. Z. El-Khoury, and W. P. Hess, Nano Lett. **15**, 3472 (2015).
[8] M. Shibuta, T. Eguchi, and A. Nakajima, Plasmonics **8**, 1411 (2013).
[9] C. Lemke, T. Leißner, A. Klick, J. Fiutowski, J. W. Radke, M. Thomaschewski, J. Kjelstrup-Hansen, H.-G. Rubahn, and M. Bauer, Appl. Phys. B **116**, 585 (2014).
[10] C. Lemke, C. Schneider, T. Leißner, D. Bayer, J. W. Radke, A. Fischer, P. Melchior, A. B. Evlyukhin, B. N. Chichkov, C. Reinhardt, M. Bauer, and M. Aeschlimann, Nano Lett. **13**, 1053 (2013).
[11] B. Frank, P. Kahl, D. Podbiel, G. Spektor, M. Orenstein, L. Fu, T. Weiss, M. H.-v. Hoegen, T. J. Davis, F.-J. M. zu Heringdorf, and H. Giessen, Sci. Adv. **3**, e1700721 (2017).
[12] M. Großmann, A. Klick, C. Lemke, J. Falke, M. Black, J. Fiutowski, A. J. Goszczak, E. Sobolewska, A. U. Zillohu, M. K. Hedayati, H.-G. Rubahn, F. Faupel, M. Elbahri, and M. Bauer, ACS Photonics **2**, 1327 (2015).
[13] T. Leißner, C. Lemke, J. Fiutowski, J. W. Radke, A. Klick, L. Tavares, J. Kjelstrup-Hansen, H.-G. Rubahn, and M. Bauer, Phys. Rev. Lett. **111**, 046802 (2013).
[14] M. Dąbrowski, Y. Dai, A. Argondizzo, Q. Zou, X. Cui, and H. Petek, ACS Photonics **3**, 1704 (2016).
[15] G. Spektor, D. Kilbane, A. K. Mahro, B. Frank, S. Ristok, L. Gal, P. Kahl, D. Podbiel, S. Mathias, H. Giessen, F.-J. M. zu Heringdorf, M. Orenstein, and M. Aeschlimann, Science **355**, 1187 (2017).
[16] J. P. S. Fitzgerald, R. C. Word, S. D. Saliba, and R. Könenkamp, Phys. Rev. B **87**, 205419 (2013).
[17] R. C. Word, J. P. S. Fitzgerald, and R. Könenkamp, Opt. Express **21**, 30507 (2013).
[18] T. Stenmark, R. C. Word, and R. Könenkamp, Opt. Express **24**, 3839 (2016).
[19] R. C. Word and R. Könenkamp, Opt. Express **24**, 18727 (2016).
[20] J. P. S. Fitzgerald, R. C. Word, and R. Könenkamp, Phys. Rev. B **89**, 195129 (2014).
[21] W. Swiech, G. Fecher, C. Ziethen, O. Schmidt, G. Schönhense, K. Grzelakowski, C. M. Schneider, R. Frömter, H. Oepen, and J. Kirschner, J. Electron Spectrosc. Relat. Phenom. **84**, 171 (1997).
[22] M. U. Wehner, M. H. Ulm, and M. Wegener, Opt. Lett. **22**, 1455 (1997).
[23] L. F. Kadem, C. Lamprecht, J. Purtov, and C. Selhuber-Unkel, Langmuir **31**, 9261 (2015).
[24] R. Williams, Phys. Rev. **140**, A569 (1965).
[25] A. M. Goodman, J. Electrochem. Soc. **115**, 276C (1968).
[26] R. Yan, Q. Zhang, W. Li, I. Calizo, T. Shen, C. A. Richter, A. R. Hight-Walker, X. Liang, A. Seabaugh, D. Jena, H. G. Xing, D. J. Gundlach, and N. V. Nguyen, Appl. Phys. Lett. **101**, 022105 (2012).
[27] A. Klick, S. de la Cruz, C. Lemke, M. Großmann, H. Beyer, J. Fiutowski, H.-G. Rubahn, E. R. Méndez, and M. Bauer, Appl. Phys. B **122**, 79 (2016).
[28] P. Welch, IEEE Trans. Audio Electroacoust. **15**, 70 (1967).
[29] G. Lifante, *Integrated Photonics: Fundamentals* (Wiley, Chichester, 2003).
[30] W. Dai and C. M. Soukoulis, Phys. Rev. B **80**, 155407 (2009).
[31] H. W. Kihm, J. H. Kang, J. S. Kyoung, K. G. Lee, M. A. Seo, and K. J. Ahn, Appl. Phys. Lett. **94**, 141102 (2009).
[32] P. Lalanne, Surf. Sci. Rep. **64**, 453 (2009).
[33] H. Liu and P. Lalanne, Phys. Rev. B **82**, 115418 (2010).
[34] C. H. Gan, L. Lalouat, P. Lalanne, and L. Aigouy, Phys. Rev. B **83**, 085422 (2011).
[35] C. Lemke, T. Leißner, A. Klick, J. W. Radke, J. Fiutowski, J. Kjelstrup-Hansen, H.-G. Rubahn, and M. Bauer, Opt. Express **21**, 27392 (2013).
[36] See Supplemental Material at http://link.aps.org/supplemental/10.1103/PhysRevB.98.085128 for a movie generated from the time-resolved data.
[37] A. D. Humphrey and W. L. Barnes, Phys. Rev. B **90**, 075404 (2014).